



Shear strain alters the structure and migration mechanism of self-interstitial atoms in copper

B. Zhang,¹ C. Wheatley ^{1,2} P. Chen,^{1,3} X. Qian,^{1,4} and M. J. Demkowicz ^{1,*}

¹Department of Materials Science and Engineering, Texas A&M University, College Station, Texas 77845, USA

²Department of Materials Science and Engineering, Penn State University, State College, Pennsylvania 16801, USA

³Key Laboratory of Automobile Materials of Ministry of Education, School of Materials Science and Engineering, Jilin University, Changchun, People's Republic of China

⁴Department of Electrical and Computer Engineering, Texas A&M University, College Station, Texas 77845, USA



(Received 17 October 2021; accepted 5 May 2022; published 17 May 2022)

We use atomistic modeling to show that externally applied shear strain causes the lowest energy self-interstitial atom (SIA) structure in copper (Cu) to change from a $\langle 100 \rangle$ -type dumbbell to a $\langle 110 \rangle$ -type dumbbell. Concurrently, SIA migration switches from the three-dimensional (3D) random walk characteristic of $\langle 100 \rangle$ -type dumbbells to a 1D mechanism analogous to that of crowdion SIAs. Furthermore, the relative energies of these two dumbbell structures as a function of strain are well predicted using elastic dipole tensors computed at zero strain, indicating that examination of these tensors may be used to assess the likelihood of strain-induced SIA structure transitions in other materials. Changes in lowest energy SIA structures and associated migration mechanisms stand to impact predictions of SIA behavior in irradiated solids.

DOI: [10.1103/PhysRevMaterials.6.053605](https://doi.org/10.1103/PhysRevMaterials.6.053605)

I. INTRODUCTION

Vacancies are the most important point defects for understanding mass transport in crystalline metals under thermodynamic equilibrium [1]. However, under irradiation, self-interstitial atoms (SIAs) play an equally significant role [2]. Understanding SIA properties is therefore essential for predicting the radiation response of metals.

Unlike vacancies, SIAs exhibit a variety of atomic structures. For example, there are six canonical SIA configurations in face centered cubic (fcc) and body centered cubic (bcc) metals: octahedral, tetrahedral, crowdion, and split dumbbell with $\langle 100 \rangle$, $\langle 110 \rangle$, or $\langle 111 \rangle$ crystallographic orientations [3]. Split-dumbbell SIAs may be viewed as defects where two atoms occupy a single lattice site. These atoms are offset from each other, with the occupied lattice site at the midpoint between them. The orientation of the defect is described by the Miller index of the line segment passing between the two atoms, giving the defect its name (e.g., in a $\langle 100 \rangle$ dumbbell, the atom pair is oriented along a crystallographic $\langle 100 \rangle$ -type direction). SIA structure determines SIA properties [4,5], e.g., diaelasticity [6,7], paraelasticity [8], and migration behavior [9–12].

The crystal structure and composition of the host lattice are thought to determine the lowest energy SIA structure. In most fcc metals, the $\langle 100 \rangle$ dumbbell has the lowest energy [9]. However, in Pt, Rh, and Th, the lowest energy SIA is octahedral, while the lowest energy structure is uncertain in several other fcc metals (Sr, Ir, Au, Pb) [9]. The lowest energy SIAs in bcc metals are usually crowdions or $\langle 111 \rangle$ dumbbells [13,14]. The exception is α -Fe, whose magnetism causes the $\langle 110 \rangle$ dumbbell to have the lowest energy among the canonical SIA

structures [15]. Moreover, the lowest energy SIAs in Cr, Mo, and W take on symmetry-broken, noncanonical forms [10].

However, recent research demonstrates that the lowest energy SIA structures are not fixed for a given element and crystal structure, but rather may depend on elastic strain. Using classical potential calculations, Kang *et al.* show that, at a critical value of externally applied strain, the lowest energy SIA structure in α -Fe shifts from the $\langle 110 \rangle$ dumbbell to a $\langle 111 \rangle$ -oriented configuration [11]. Concurrently, the SIA migration pattern changes from a three-dimensional (3D) random walk characteristic of the conventional $\langle 110 \rangle$ dumbbell to a 1D random walk reminiscent of that seen in other bcc metals [12], albeit with higher activation energy. Similarly, Suzudo and Tsuru find that strain may stabilize symmetry-broken SIA structures in W [16].

The present work investigates the effect of externally applied shear strain on lowest energy SIA structures in fcc Cu. Based on both density functional theory (DFT) and classical potential calculations, we find that, up to a simple shear strain of $\sim 3\%$, the lowest energy structure is the $\langle 100 \rangle$ dumbbell, as expected [9]. However, at higher strains, the $\langle 110 \rangle$ dumbbell has the lowest energy. This change in the lowest energy structure is accompanied by a transition from 3D migration to 1D migration with significantly reduced activation energy. Our results suggest that strain-induced changes in lowest energy SIA structures and associated modifications in migration behavior may be common to many metals. Finally, we discuss the potential implications of these findings for understanding SIA behavior in irradiated metals.

II. MODELING METHODS

Defect formation and migration energies are determined using DFT as well as classical potential calculations. In both cases, we use a simulation cell consisting of a $4 \times 4 \times 4$ grid

*Corresponding author: demkowicz@tamu.edu

of cubic unit cells of fcc Cu under periodic boundary conditions. The initial dimensions of the model are set to ensure zero pressure at zero temperature. Upon addition of one SIA, the model contains 257 atoms. To impose a simple shear strain ϵ_{xy} on the model, we change the shape of the simulation cell by applying the deformation gradient

$$F = \begin{bmatrix} 1 & \epsilon_{xy} & 0 \\ 0 & 1 & 0 \\ 0 & 0 & 1 \end{bmatrix}. \quad (1)$$

We perform DFT simulations [17,18] using the Vienna Ab initio Simulation Package (VASP) [19]. The calculations apply the Perdew-Burke-Ernzerhof (PBE) [20] form of the exchange-correlation functional within the generalized gradient approximation (GGA) [21] and a plane wave basis set with a 400 eV energy cutoff. Structural optimization and electronic relaxation are calculated using a Γ -centered Monkhorst-Pack [22] k -point sampling grid of $3 \times 3 \times 3$. The maximal residual force of each atom is $0.01 \text{ eV } \text{\AA}^{-1}$, and the convergence threshold for electronic relaxation is 10^{-6} eV .

Classical potential calculations are carried out using the LAMMPS code [23]. Atomic interactions are modeled using an embedded atom method (EAM) [24] potential for Cu developed by Mishin *et al.* [25]. Stable defect states are relaxed using the conjugate gradient (CG) method. Transition states are found using the nudged elastic band (NEB) method [26,27]. Atomic structures are visualized using the ATOMEYE software [28].

Formation energies are computed as

$$\Delta E^f = E_{\text{defect}}(\epsilon) - \frac{N}{N-1} E_{\text{perfect}}(\epsilon), \quad (2)$$

where $E_{\text{defect}}(\epsilon)$ is the energy of the model containing a SIA, $E_{\text{perfect}}(\epsilon)$ is the energy of the perfect single crystal model with no defect, and N is the total number of atoms in the model containing a SIA (thus, $N-1$ is the number of atoms in the single crystal model). Both $E_{\text{defect}}(\epsilon)$ and $E_{\text{perfect}}(\epsilon)$ are computed at the same applied strain, ϵ . SIA elastic dipole tensors, i.e., P tensors, are computed from the residual stress $\langle \sigma_{ij} \rangle$ generated by the defect [29]:

$$P_{ij} = -V \sigma_{ij}. \quad (3)$$

Here, V is the model volume.

Defect diffusivity tensors are obtained using molecular dynamics (MD) simulations on a fcc Cu model with its lattice rotated such that $\langle 110 \rangle$ -type (face diagonal) directions are aligned with the x and y coordinate axes, and a $\langle 100 \rangle$ -type direction is aligned with the z coordinate axis. The model is under periodic boundary conditions and contains 4951 atoms after a SIA is added. In this rotated lattice, strains equivalent to the simple shear used in the smaller model discussed above are obtained by imposing a biaxial shape change on the simulation cell described by the deformation gradient,

$$F = \begin{bmatrix} \sqrt{1 + \epsilon_{xy} + \frac{1}{2}\epsilon_{xy}^2} & 0 & 0 \\ 0 & \sqrt{1 - \epsilon_{xy} + \frac{1}{2}\epsilon_{xy}^2} & 0 \\ 0 & 0 & 1 \end{bmatrix}. \quad (4)$$

For every temperature of interest, the volume of the model is adjusted to allow for thermal expansion. Atom trajectories

are subsequently generated under the NVE ensemble for a total of time of 2 ns. The generalized mean square displacement (MSD) per atom matrix,

$$G_{\text{MSD}} = \frac{1}{N} \begin{bmatrix} \sum_{i=1}^N \Delta x_i^2 & \sum_{i=1}^N \Delta x_i \Delta y_i & \sum_{i=1}^N \Delta x_i \Delta z_i \\ \dots & \sum_{i=1}^N \Delta y_i^2 & \sum_{i=1}^N \Delta y_i \Delta z_i \\ \dots & \dots & \sum_{i=1}^N \Delta z_i^2 \end{bmatrix}, \quad (5)$$

is computed periodically throughout the simulation and recorded. $(\Delta x_i, \Delta y_i, \Delta z_i)$ denote displacements of individual atoms from their initial positions. Ellipses indicate that the matrix is symmetric about its diagonal. A sample script for calculating G_{MSD} is provided in the Supplemental Material [30].

According to the Einstein relation, the diffusivity matrix D is related to G_{MSD} through $2Dt = G_{\text{MSD}}$ in the limit of a long time, t . We obtain the individual elements of D from linear least-squares fits to the corresponding elements of G_{MSD} over time. The first 1 ps of the simulation is excluded from the fit to allow for the ballistic stage of the MSD calculation. The diffusivity thereby obtained is the SIA diffusivity, not the self-diffusivity of Cu, because G_{MSD} is computed on a per-atom basis, and the SIA is the only significant source of atom mobility in the model. Data sets that yield negative diffusivities are excluded from further analysis.

Diffusivities are calculated for ϵ_{xy} values ranging from 0 to 0.08 in increments of 0.01 over temperatures from 200 to 700 K in increments of 100 K. For ϵ_{xy} of 0.03 and above, diffusivities are additionally calculated for temperatures of 250, 350, and 450 K. Seven independent simulations with different initial velocity distributions are conducted for each strain/temperature combination to ensure acceptable statistics. Effective activation energies for diffusion, ΔE_{ij} , along with corresponding uncertainties are obtained by fitting the Arrhenius form, $D_{ij} = D_{ij}^0 e^{-\Delta E_{ij}/k_B T}$, via linear regression of the logarithm of individual diffusivity components against the inverse of the thermal energy, $1/k_B T$. The analysis also returns the logarithm of the diffusivity prefactor, D_{ij}^0 .

III. STRAIN-INDUCED STRUCTURE TRANSITION

Figure 1(a) shows a relaxed $[100]$ dumbbell SIA in strain-free fcc Cu, as modeled by DFT. We apply simple shear

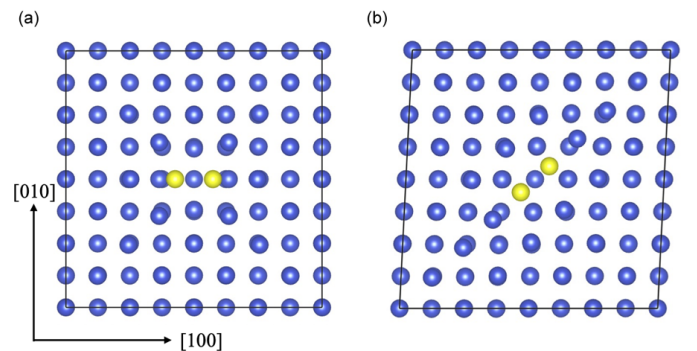


FIG. 1. Relaxed SIA structures as modeled by DFT: (a) $[100]$ dumbbell zero strain and (b) $[110]$ dumbbell at a strain of 0.05. The two SIA core atoms are colored yellow.

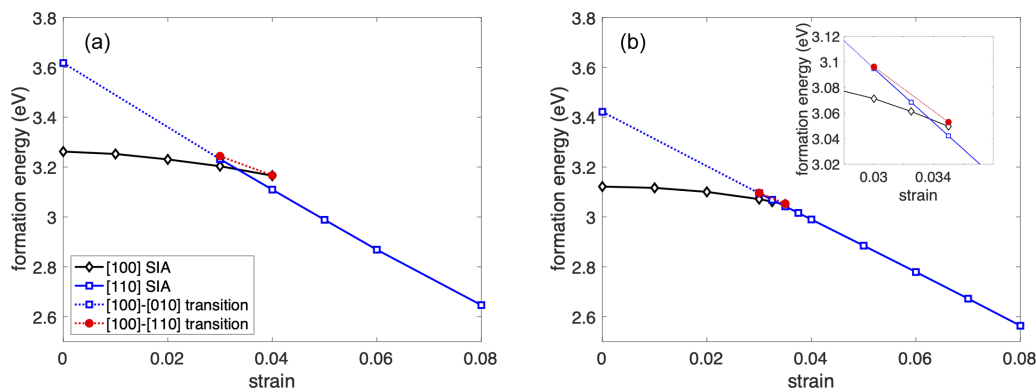


FIG. 2. SIA energies computed as a function of strain using (a) DFT and (b) the classical EAM potential of Mishin *et al.* [25]. The legend shown in (a) applies to (b), as well. The inset in (b) shows a magnified view of the region where both [100] and [110] dumbbell structures are stable.

strains to this initial structure in increments of 0.01, relaxing the structure after each loading step. The [100] dumbbell SIA remains stable up to a strain of 0.04. Upon reaching a strain of 0.05, it relaxes spontaneously into the [110] dumbbell configuration shown in Fig. 1(b) and remains in this structure up to the maximum strain modeled here, namely 0.08. We then gradually unload this structure, reducing the strain in increments of 0.01 and relaxing after each increment. The [110] dumbbell remains stable down to a strain of 0.03. Upon reaching a strain of 0.02, it transforms spontaneously into the [110] dumbbell configuration.

Figure 2(a) summarizes the formation energies of both [100] and [110] dumbbells over their respective ranges of stability, as determined by DFT. The energy of the transition state for rotation of a [100] dumbbell into a [010] orientation at zero strain is also shown. This transition state has the structure of a [110] dumbbell. When extrapolated to zero strain, a line drawn through the formation energies of stable [110] dumbbells at higher strains virtually intersects with the zero strain [100]-[010] transition energy. The plot also shows the energies of transition states from the [100] dumbbell to a [110] dumbbell at strains of 0.03 (activation energy ≈ 4 meV) and 0.04 (activation energy ≈ 0.1 meV), where both configurations are stable.

Figure 2(b) shows the same data as Fig. 2(a), but computed using the classical potential of Mishin *et al.* [25]. Despite some quantitative differences (most notably, all formation energies are approximately 0.1 eV lower than the corresponding DFT values), the classical potential results are in excellent qualitative agreement with DFT. The [100] dumbbell remains

the lowest energy structure up to a strain of 0.035 and relaxes to a [110] dumbbell at strains of 0.04 and above. The [110] dumbbell remains stable down to strains of 0.03 and relaxes to the [100] dumbbell configuration at lower strains. The transition state of the [100]-[010] rotation at zero strain has the structure of a [110] dumbbell and an energy that lies on the same trendline of stable [110] dumbbells at higher strains. Activation energies for [100]-[110] transitions at strains of 0.03 and 0.035 (where both SIA structures are stable) are 2.5 and 1 meV, respectively.

The trends in defect formation energies shown in Fig. 2 are reasonably well predicted from P tensors computed at zero strain. The values of these tensors for both [100] and [110] dumbbells are reported in Table I. The zero-strain P tensor for the [110] dumbbell is calculated at the saddle point configuration for rotation of a [100] dumbbell into a [010] orientation. Given the formation energy of a defect at zero strain, $\Delta E^f(0)$, the formation energy at nonzero strain $\Delta E^f(\epsilon)$ is computed as

$$\Delta E^f(\epsilon) = \Delta E^f(0) - P_{ij}\epsilon_{ij}. \quad (6)$$

Summation over repeated indices is implied. In our calculations, there is only one nonzero component of strain (ϵ), so the expression above reduces to $\Delta E^f(\epsilon) = \Delta E^f(0) - P_{12}\epsilon_{12}$.

Figure 3 compares the formation energies of [100] and [110] dumbbells calculated using VASP and LAMMPS with those obtained from P tensors. In both cases, P tensors predict that the formation energy of the [110] dumbbell drops below that of the [100] dumbbell at a strain of approximately 0.03, in good agreement with atomistic calculations. Because all the off-diagonal elements of the [100] dumbbell P tensor are

TABLE I. Elastic dipole tensors (P tensors) computed at zero strain for both [100] and [110] dumbbells using DFT (VASP) and the classical EAM potential of Mishin *et al.* [25] (LAMMPS). Tensor components have units of eV.

Dumbbell type	DFT	EAM
[100]	$\begin{bmatrix} 19.361 & 0 & 0 \\ 0 & 19.470 & 0 \\ 0 & 0 & 19.470 \end{bmatrix}$	$\begin{bmatrix} 18.515 & 0 & 0 \\ 0 & 19.959 & 0 \\ 0 & 0 & 19.959 \end{bmatrix}$
[110]	$\begin{bmatrix} 19.150 & 12.460 & 0.0220 \\ 12.460 & 19.150 & 0.0220 \\ 0.0220 & 0.0220 & 21.435 \end{bmatrix}$	$\begin{bmatrix} 18.275 & 10.447 & 0 \\ 10.447 & 18.275 & 0 \\ 0 & 0 & 21.543 \end{bmatrix}$

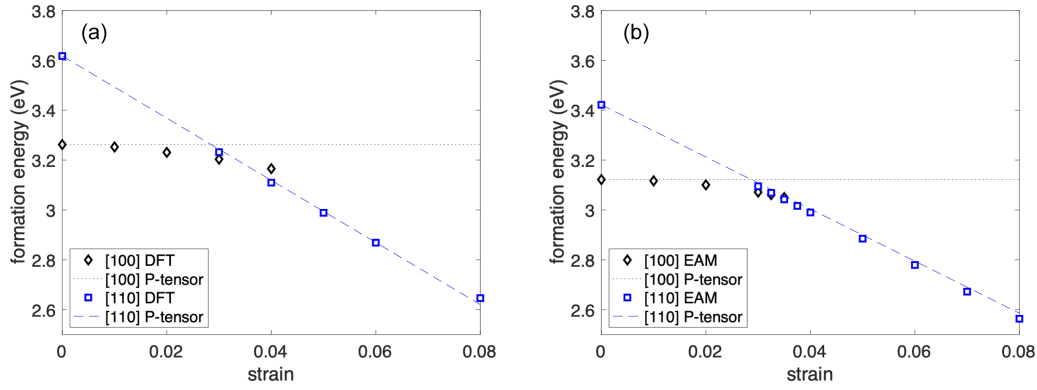


FIG. 3. Comparison of formation energies of [100] and [110] dumbbells calculated using (a) DFT and (b) EAM with those obtained from the corresponding P tensors (see Table I).

zero, Eq. (6) predicts that the formation energy of this SIA structure has no first order (linear) dependence on shear strain. However, the atomistic calculations suggest that there is a second order (quadratic) dependence on shear strain, tending to decrease the [100] dumbbell formation energy. Such a dependence may be captured using the polarizability tensor of the [100] dumbbell [29].

IV. EFFECT OF STRAIN ON DIFFUSIVITY

Figure 4 shows an example, taken from $T = 700$ K, of the variation of all six independent components of the SIA diffusivity tensor with strain. Plots made for other temperatures exhibit the same qualitative features. At all strains, $D_{xy}, D_{xz}, D_{yz} \approx 0$, meaning that the coordinate system used in all these simulations is the principal coordinate system for diffusivity. At zero strain $D_{xx} \approx D_{yy} \approx D_{zz}$, i.e., diffusivity is isotropic. This finding is consistent with the known 3D diffusion mechanism of $\langle 100 \rangle$ -type dumbbells in Cu, the lowest energy SIA structures at zero strain [31].

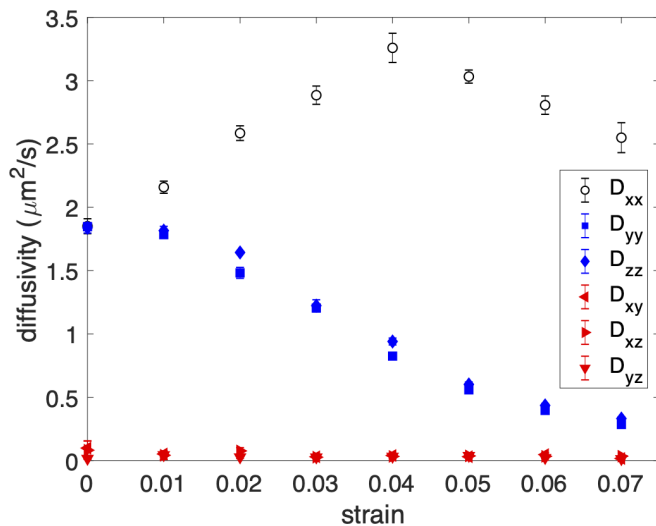


FIG. 4. The variation of all six independent SIA diffusivity tensor components with strain at 700 K. When error bars are not visible, it is because they are smaller than the symbols used for plotting.

With increasing strain, $D_{yy} \approx D_{zz}$ decrease monotonically while D_{xx} increases up to a strain of 0.04. Thereafter, it gradually decreases but remains substantially higher than D_{yy} and D_{zz} . Thus, SIA diffusivity at nonzero strain is anisotropic. The fastest diffusion direction is the x direction. In our model, this direction corresponds to a [110] crystallographic axis. Under the deformation gradient applied in our simulations (see Sec. II), it is elongated for any positive value of applied strain.

For strains up to ~ 0.03 , the anisotropic diffusivity shown in Fig. 4 may be attributed to the strain sensitivity of the migration energy of $\langle 100 \rangle$ -type dumbbells, as characterized by Vattré *et al.* [31]. Thus, SIA migration remains 3D but is biased by strain to occur preferentially along the x direction. Above strains of ~ 0.04 , the stable SIA structure is the [110] dumbbell aligned with the x direction. The fast diffusivity of this defect arises from crowdionlike, 1D mobility along the x direction and the relative difficulty of reorientations to other directions. At strains between 0.03 and 0.04, both $\langle 100 \rangle$ -type and [110] dumbbells are stable and of comparable formation energy. Thus, both may contribute to diffusivity.

The foregoing interpretation is supported by the effective activation energies for SIA migration shown in Fig. 5(a). Up to a strain of ~ 0.03 , the activation energies for migration in the y and z directions (ΔE_{yy} and ΔE_{zz}) remain nearly unchanged while that for migration along the x direction (ΔE_{xx}) decreases gradually. For strains of 0.04 and above, ΔE_{yy} and ΔE_{zz} are about an order of magnitude higher than ΔE_{xx} , signaling a transition from 3D diffusion of $\langle 100 \rangle$ -type dumbbells to 1D diffusion of the [110] dumbbell. For completeness, Fig. 5(b) shows the diffusivity prefactors obtained for each component by fitting to the Arrhenius expression. The elevated values of D_{yy}^0 and D_{zz}^0 for strains of 0.04–0.06 are accompanied by markedly heightened uncertainties, suggesting that our statistical sample may be inadequate for inferring these two quantities via regression analysis in this strain range.

The effective migration energy at zero strain shown in Fig. 5(a) is consistent with previous NEB calculations of $\langle 100 \rangle$ -type dumbbell migration in Cu [31]. To further investigate 1D diffusivity at strains of 0.03–0.05, we carried out NEB calculations for [110] dumbbell migration using both DFT and classical potential calculations. Figure 6(a) shows an example minimum energy path computed at 0.04 strain using DFT (paths computed at other strains are qualitatively simi-

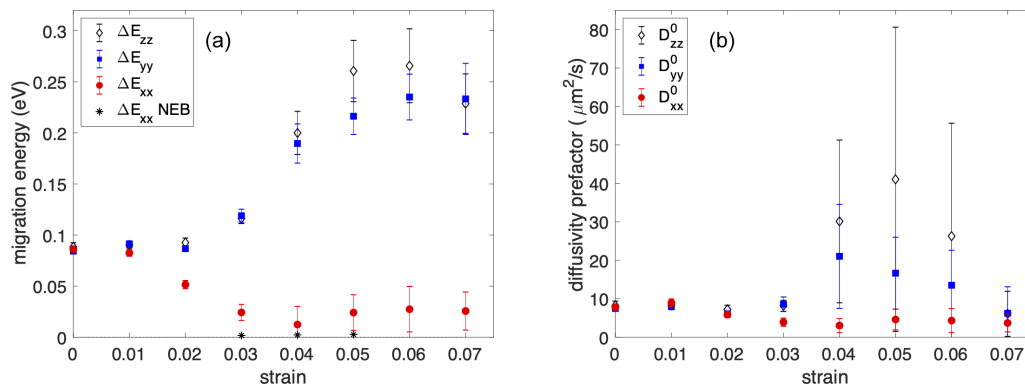


FIG. 5. (a) Effective activation energies and (b) diffusivity prefactors for SIA migration as a function of strain obtained from linear regression of the Arrhenius form for diffusivity.

lar). The midpoint of the path is a shallow potential energy minimum corresponding to a metastable crowdion structure. The activation energy for migration is taken to be the highest energy along this path. Figure 6(b) shows an example minimum energy path obtained from the classical potential. In this case, the crowdion structure at the midpoint is unstable and corresponds to the highest energy along the path.

Table II reports the migration activation energies obtained by DFT and the classical potential. There is a significant disparity between them, with the DFT values being systematically higher. Overall, there is both qualitative and quantitative disagreement between DFT and the classical potential for 1D [110] dumbbell migration. Finally, the activation energies found from the classical potential using NEB are plotted in Fig. 5(a). They are substantially lower than the activation energies inferred by linear regression on diffusivity data. This finding appears consistent with the observation of Derlet *et al.* [12], who suggested that the temperature dependence of diffusivity for 1D SIA migration does not arise from thermal activation, as assumed by the Arrhenius relation, but rather from interactions of the SIA with phonons.

V. DISCUSSION

We have demonstrated that the lowest energy self-interstitial atom (SIA) structure in Cu changes from the [100] dumbbell to the [110] dumbbell under an externally applied shear strain. The strain dependence of the relative formation energies of these two SIA structures are well predicted by elastic dipole tensors (P tensors) computed at zero strain. The transition in SIA structure is accompanied by a change in migration mechanism, from isotropic, 3D migration of the [100] dumbbell at zero strain to anisotropic, 1D migration of the

[110] dumbbell. DFT calculations are in excellent agreement with the EAM classical potential of Mishin *et al.* [25], except for the 1D migration path of the [110] dumbbell, where the potential fails to reproduce the metastability of the intermediate crowdion structure and underpredicts the migration energy.

The configuration of strain-dependent equilibrium paths (both stable and unstable) of the SIA structures summarized in Fig. 2 may be illustrated schematically using a bifurcation diagram, as shown in Fig. 7. The horizontal axis represents strain, while the vertical axis stands for all the internal variables (i.e., atomic positions) that describe changes in SIA structure. Following the terminology of elastic stability theory [32], the termination of the stable branch of the [100] dumbbell (as well as that of the symmetry-related [010] dumbbell) is classified as a saddle-node or fold instability. In it, the stable equilibrium path corresponding to the [100] dumbbell joins with the unstable equilibrium path constituted by the saddle point configurations along the [100]-[110] transition. The point where the stable and unstable paths meet corresponds to the strain at which the activation energy for the [100]-[110] transition vanishes, marking the end of stability of the [100] dumbbell.

The unstable branch of the [110] dumbbell becomes stable at its intersection with the two unstable branches of the [100] and [010] dumbbells. This point is known as pitchfork instability. At strains below this point, the unstable [110] branch is the saddle point configuration of the [100]-[010] transition. Pitchfork instabilities are often destroyed by perturbations that break an underlying symmetry, in this case, the structural equivalence of the symmetry-related [100] and [010] dumbbells. For example, we may anticipate that the bifurcation diagram in Fig. 7 will change its topology under a uniaxial prestrain along the [100] direction.

The predicted transition between SIA structures occurs at lattice shear strains of ~ 0.04 , corresponding to shear stresses of ~ 3 GPa in Cu. Such stresses far exceed the yield strength of polycrystalline pure Cu, which is on the order of 0.03 GPa, as well as those of Cu alloys, such as brass or bronze, which are usually lower than 0.2 GPa. Therefore, on the grain scale, plastic flow prevents lattice strains from reaching levels capable of causing a change in SIA structure. However, local stresses in the vicinity of defects, such as dislocations [33], voids [34], cracks [35], or interfaces [36], may easily exceed 3 GPa. Strain-induced changes in SIA structure are therefore likeliest to occur in near such defects.

TABLE II. Activation energies (in eV) for 1D [110] dumbbell migration at a strain of 0.04 obtained by NEB using DFT (VASP) and EAM classical potential calculations (LAMMPS).

Strain	DFT	EAM
0.03	0.0835	0.0017
0.04	0.0790	0.0022
0.05	0.0748	0.0027

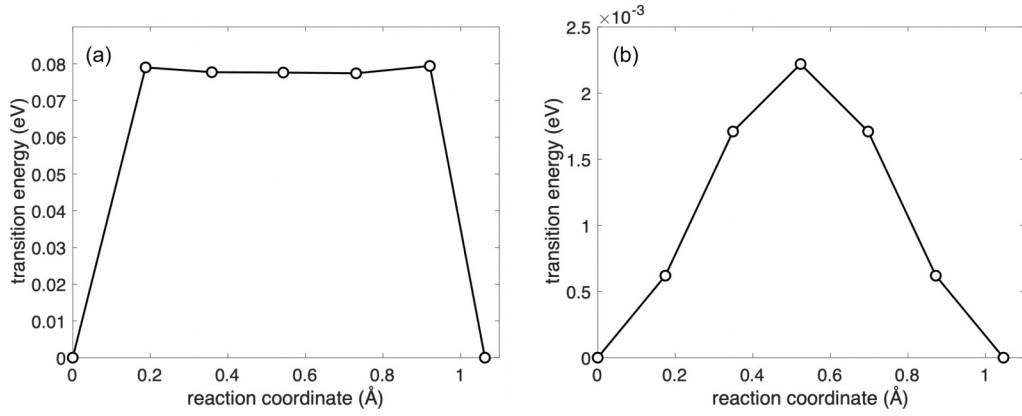


FIG. 6. Minimum energy paths for 1D [110] dumbbell migration at a strain of 0.04 obtained by NEB using (a) DFT (VASP) and (b) classical potential calculations (LAMMPS).

Local strains near defects are rarely ever single-component pure shear. Rather, they take on general tensorial form with all six independent strain components having nonzero values. In such cases, lowest energy SIA structures are most conveniently predicted using P tensors. By way of example, consider a helium (He) bubble: a spherical cavity of radius R filled with He gas at pressure p . Nanoscale He bubbles are a well-known form of radiation-induced damage in metals [37]. In a suitably chosen coordinate system, linear isotropic continuum elasticity theory predicts that the strain at a distance $r > R$ from the bubble center is [38]

$$\varepsilon = \frac{pR^3}{4\mu r^3} \begin{bmatrix} 0 & 1 & 1 \\ 1 & 0 & 1 \\ 1 & 1 & 0 \end{bmatrix}, \quad (7)$$

where μ is the shear modulus of the metal. Thus, the strain around the bubble is a superposition of three equal pure shears. Provided that P tensors and strains are expressed in the same coordinate system, the combined effect of all three shears on the formation energies of all [100] and [110] dumb-

bell variants may be computed directly using Eq. (6). The variant with lowest formation energy may then be identified.

We followed this approach to determine lowest energy SIA structures for a bubble with $R = 5$ nm and $p = 5$ GPa (He bubbles may sustain internal pressures in excess of 15 GPa [39]) in a Cu matrix with $\mu = 44$ GPa. We used the P tensors computed from classical potentials listed in Table I (rotated as needed for the remaining two [100]-type and five [110]-type SIA variants). We found that such a bubble is surrounded by lobes of volume where a [110] dumbbell variant is the lowest energy SIA structure, as shown in Fig. 8. Similar calculations may easily be carried out for local strain distributions around other types of defects.

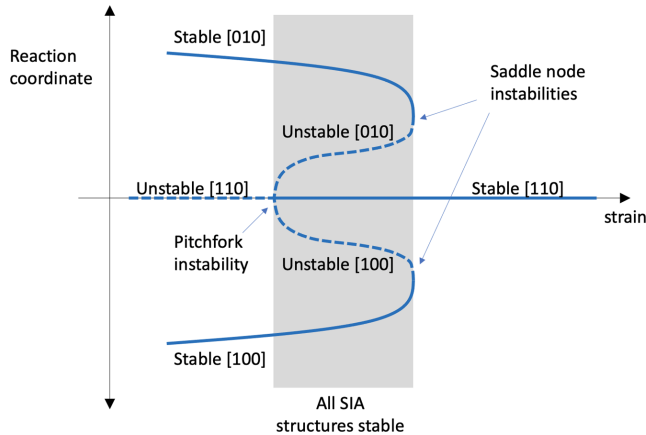


FIG. 7. Bifurcation diagram of strain-dependent equilibrium paths for [100], [010], and [110] dumbbells in Cu. The horizontal axis represents externally applied strain, while the vertical axis stands for all the internal variables associated with changes in SIA structure.

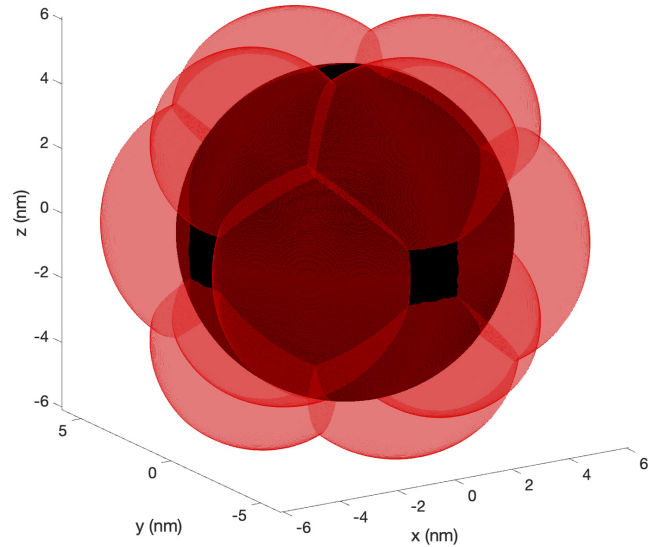


FIG. 8. The opaque, black surface represents a He bubble with $R = 5$ nm and $p = 5$ GPa. The semitransparent, red lobes indicate regions within which local strains cause a [110]-type dumbbell variant to become the lowest energy SIA structure. The Cartesian axes are aligned with (100)-type Miller index directions. Two [110]-type dumbbell variants have degenerate energies at surfaces where two lobes meet. Three [110]-type dumbbell variants have degenerate energies at lines where three lobes meet. Outside of the lobes, the lowest energy SIAs are [100]-type dumbbell variants.

Strain-induced transitions in the lowest energy SIA structure and associated changes in diffusivity have the potential to impact models of radiation response. While virtually absent under thermal equilibrium, SIAs are created in high concentrations under irradiation. Their fate affects technologically important material behaviors, such as swelling [40], creep [41], and embrittlement [42]. These phenomena depend on the interactions of SIAs with other defects (e.g., vacancies or dislocations) as well as sinks, such as voids or interfaces. Strain-induced alterations of SIA formation and migration energies have a significant impact on these interactions [31,34,43]. For example, the changes in SIA structure predicted in Fig. 8 are likely to modify SIA capture rates at He bubbles by altering SIA migration paths near bubble surfaces. However, to date, no models have accounted for such strain-induced changes in SIA structure. P tensors may provide a facile means to incorporate this additional physics into object kinetic Monte Carlo (OKMC) models [44].

Strain-induced stabilization of the [110] dumbbell and consequent 1D migration may also explain the occurrence of long-range vacancy/SIA recombination along $\langle 110 \rangle$ -type directions. Such long-range recombination events are observed in single crystal Cu [45,46] as well as near grain boundaries [46,47] and heterophase interfaces [45]. In such cases, the vacancy acts as a center of negative dilatation, generating a shear strain field in its vicinity [48]. While this field's intensity dies down rapidly with distance from the vacancy, the strength of its interaction with nearby SIAs may be sufficient to induce a change from a $\langle 100 \rangle$ -type to a $\langle 110 \rangle$ -type structure. If the $\langle 110 \rangle$ -type dumbbell and the vacancy lie along the same $\langle 110 \rangle$ -oriented atom column, the SIA may move towards the vacancy via 1D migration, eventually recombining with it.

The effect of strain on vacancy/SIA reactions may be predicted by computing vacancy/SIA interaction energies, $\Delta E_{v/SIA}$. To first order [49],

$$\Delta E_{v/SIA} = P_{li}^v P_{kj}^{SIA} G_{ij,kl}(\vec{r}) \quad (8)$$

where P_{li}^v and P_{kj}^{SIA} are the P tensors of the vacancy and SIA, respectively, and $G_{ij,kl}(\vec{r})$ is the second derivative of the elastic Green's function tensor as a function of the relative position of the vacancy and SIA, \vec{r} . We use this relation to compute the formation energy of vacancy/[100] dumbbell and vacancy/[110] dumbbell pairs as a function of separation along the [110] direction. For this calculation, we adopt the SIA P tensors computed from classical potentials and listed in Table I. For the vacancy, we calculate $\Delta E_f^v = 1.27$ eV and $P^v = -3.03I$ eV. We use the Green's function for an isotropic, linear elastic, continuum solid [50] with Cu represented by $\nu = 0.34$, $\mu = 44$ GPa.

Figure 9 shows the outcome of this calculation. Despite the 0.3-eV difference between the formation energies of [100] and [110] dumbbells at zero strain, the elastic interaction between a vacancy and a SIA causes the [110] dumbbell to become

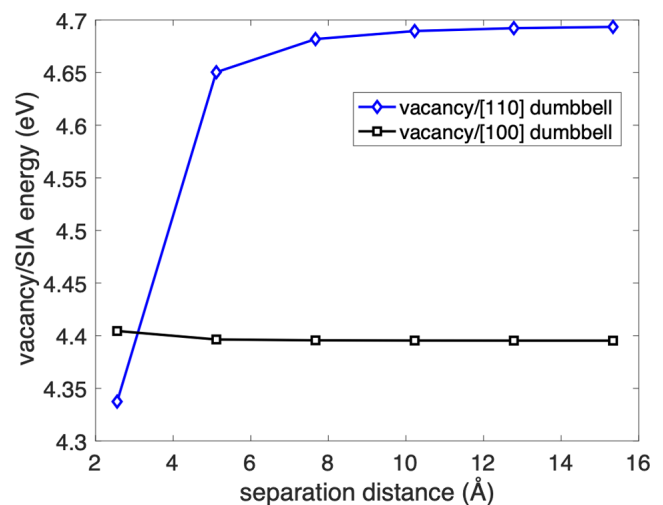


FIG. 9. The effect of elastic interaction on the energy of vacancy/SIA pairs as a function of separation distance.

more stable when the vacancy and SIA are separated by one nearest neighbor distance. This calculation demonstrates that elastic interaction with a vacancy is capable in principle of causing changes in SIA structure. However, it does not account for the range of vacancy/SIA recombination along $\langle 110 \rangle$ -type directions in single-crystal Cu, which occurs at separation as high as three nearest neighbor distances [46]. Further investigation of this effect calls for more sophisticated calculations that use an elastically anisotropic lattice Green's function, account for higher moments of the multipole expansion [49], and include inhomogeneity interactions [48].

Our work is a further example (after Kang *et al.* [11] and Suzudo and Tsuru [16]) of a strain-induced change of the lowest energy SIA structure in a transition metal and the first in an fcc metal. It stands to reason that such transitions also occur in other metals and—in light of our findings—that their incidence may be identified through an analysis of zero-strain formation energies and P tensors. It may also be worth exploring whether other externally applied fields (besides strain) induce changes in SIA structure. One example might be magnetic fields applied to ferromagnetic metals, such as α -Fe, Ni, or Cr. Indeed, magnetism is believed to be a key factor stabilizing the [110] dumbbell SIA structure in α -Fe [13].

ACKNOWLEDGMENTS

DFT simulations were supported by the National Science Foundation under Award No. DMR-1753054. Classical potential simulations were supported by the U.S. Department of Energy, National Nuclear Security Administration under Award No. DE-NA0003857. Computational resources were provided by the Texas A&M High Performance Research Computing (HPRC) Center.

- [1] D. A. Porter, K. E. Easterling, and M. Y. Sherif, *Phase Transformations in Metals and Alloys*, 3rd ed. (CRC, Boca Raton, FL, 2009).
- [2] G. S. Was, *Fundamentals of Radiation Materials Science: Metals and Alloys* (Springer, Berlin, 2007).

- [3] P. Ehrhart, in *Atomic Defects in Metals*, edited by H. Ullmaier (Springer-Verlag, Berlin, 1991), p. 389–391.
- [4] W. Schilling, *J. Nucl. Mater.* **69-70**, 465 (1978).
- [5] W. G. Wolfer, *Comprehensive Nuclear Materials* **1**, 1 (2012).

- [6] L. E. Rehn, J. Holder, A. V. Granato, R. R. Coltman, and F. W. Young, *Phys. Rev. B* **10**, 349 (1974).
- [7] B. Igarashi, E. C. Johnson, and A. V. Granato, *Phys. Rev. B* **48**, 2909 (1993).
- [8] J. L. Snoek, *Physica* **8**, 711 (1941).
- [9] P. W. Ma and S. L. Dudarev, *Phys. Rev. Mater.* **5**, 013601 (2021).
- [10] P. W. Ma and S. L. Dudarev, *Phys. Rev. Mater.* **3**, 043606 (2019).
- [11] C. W. Kang, Q. Y. Wang, and L. Shao, *J. Nucl. Mater.* **485**, 159 (2017).
- [12] P. M. Derlet, D. Nguyen-Manh, and S. L. Dudarev, *Phys. Rev. B* **76**, 054107 (2007).
- [13] D. Nguyen-Manh, A. P. Horsfield, and S. L. Dudarev, *Phys. Rev. B* **73**, 020101 (2006).
- [14] D. Nguyen-Manh, S. L. Dudarev, and A. P. Horsfield, *J. Nucl. Mater.* **367–370**, 257 (2007).
- [15] F. Chu-Chun, F. Willaime, and P. Ordejon, *Phys. Rev. Lett.* **92**, 175503 (2004).
- [16] T. Suzudo, and T. Tsuru, *AIP Adv.* **11**, 065012 (2021).
- [17] P. Hohenberg and W. Kohn, *Phys. Rev.* **136**, B864 (1964).
- [18] W. Kohn and L. J. Sham, *Phys. Rev.* **140**, A1133 (1965).
- [19] G. Kresse and J. Furthmuller, *Phys. Rev. B* **54**, 11169 (1996).
- [20] J. P. Perdew, K. Burke, and M. Ernzerhof, *Phys. Rev. Lett.* **77**, 3865 (1996).
- [21] D. C. Langreth and M. J. Mehl, *Phys. Rev. B* **28**, 1809 (1983).
- [22] H. J. Monkhorst and J. D. Pack, *Phys. Rev. B* **13**, 5188 (1976).
- [23] S. Plimpton, *J. Comput. Phys.* **117**, 1 (1995).
- [24] M. S. Daw and M. I. Baskes, *Phys. Rev. B* **29**, 6443 (1984).
- [25] Y. Mishin, M. J. Mehl, D. A. Papaconstantopoulos, A. F. Voter, and J. D. Kress, *Phys. Rev. B* **63**, 224106 (2001).
- [26] G. Henkelman, B. P. Uberuaga, and H. Jonsson, *J. Chem. Phys.* **113**, 9901 (2000).
- [27] G. Henkelman and H. Jonsson, *J. Chem. Phys.* **113**, 9978 (2000).
- [28] J. Li, *Model. Simul. Mater. Sci. Eng.* **11**, 173 (2003).
- [29] E. Clouet, C. Varvenne, and T. Jourdan, *Comput. Mater. Sci.* **147**, 49 (2018).
- [30] See Supplemental Material at <http://link.aps.org/supplemental/10.1103/PhysRevMaterials.6.053605> for Sample LAMMPS script for SIA MSD calculation (see Eqn. 5).
- [31] A. J. Vattré, T. Jourdan, H. Ding, M. C. Marinica, and M. J. Demkowicz, *Nat. Commun.* **7**, 10424 (2016).
- [32] J. M. T. Thompson and G. W. Hunt, *A General Theory of Elastic Stability* (Wiley, New York, 1973).
- [33] J. P. Hirth and J. Lothe, *Theory of Dislocations*, 2nd ed. (Wiley, New York, 1982).
- [34] D. Carpentier, T. Jourdan, Y. Le Bouar, and M. C. Marinica, *Acta Mater.* **136**, 323 (2017).
- [35] K. B. Broberg, *Cracks and Fracture* (Academic, New York 1999).
- [36] N. Abdolrahim and M. J. Demkowicz, *Comput. Mater. Sci.* **118**, 297 (2016).
- [37] H. Trinkaus and B. N. Singh, *J. Nucl. Mater.* **323**, 229 (2003).
- [38] W. S. Slaughter, *The Linearized Theory of Elasticity* (Birkhäuser, Boston, 2002).
- [39] A. Caro, J. Hetherly, A. Stukowski, M. Caro, E. Martinez, S. Srivilliputhur, L. Zepeda-Ruiz, and M. Nastasi, *J. Nucl. Mater.* **418**, 261 (2011).
- [40] L. K. Mansur, *Nucl. Technol.* **40**, 5 (1978).
- [41] K. Ehrlich, *J. Nucl. Mater.* **100**, 149 (1981).
- [42] G. R. Odette and G. E. Lucas, *JOM* **53**, 18 (2001).
- [43] T. Jourdan and A. Vattré, *Comput. Mater. Sci.* **153**, 473 (2018).
- [44] G. Subramanian, D. Perez, B. P. Uberuaga, C. N. Tome, and A. F. Voter, *Phys. Rev. B* **87**, 144107 (2013).
- [45] M. J. Demkowicz, J. Wang, and R. G. Hoagland, in *Dislocations in Solids*, edited by J. P. Hirth (Elsevier, Amsterdam, 2008), p. 143–205.
- [46] M. J. Demkowicz, O. Anderoglu, X. Zhang, and A. Misra, *J. Mater. Res.* **26**, 1666 (2011).
- [47] X. M. Bai, A. F. Voter, R. G. Hoagland, M. Nastasi, and B. P. Uberuaga, *Science* **327**, 1631 (2010).
- [48] J. D. Eshelby, *Solid State Phys.* **3**, 79 (1956).
- [49] P. H. Dederichs, C. Lehmann, H. R. Schober, A. Scholz, and R. Zeller, *J. Nucl. Mater.* **69**, 176 (1978).
- [50] M. Kachanov, B. Shafiro, and I. Tsukrov, *Handbook of Elasticity Solutions* (Kluwer, Dordrecht, 2003).